AGU PUBLICATIONS

JGR

Journal of Geophysical Research: Oceans

RESEARCH ARTICLE

10.1002/2015JC011009

Seismic reflection imaging of mixing processes in Fram Strait

Sudipta Sarkar[1], Katy L. Sheen[2,3], Dirk Klaeschen[1], J. Alexander Brearley[4], Timothy A. Minshull[2], Christian Berndt[1], Richard W. Hobbs[5], and Alberto C. Naveira Garabato[2]

[1]GEOMAR Helmholtz Centre for Ocean Research, Kiel, Germany, [2]National Oceanography Centre Southampton, University of Southampton, Southampton, UK, [3]Met Office Hadley Centre, Exeter, UK, [4]British Antarctic Survey, Cambridge, UK, [5]Earth Sciences Department, Durham University, Durham, UK

Key Points:
- Seismic imaging is used to reveal oceanic fine structure to the west of Svalbard
- Isopycnal interleaving between warm Atlantic and colder Polar water on the shelf
- On the upper slope, semidiurnal internal tidal beams are seismically imaged

Correspondence to:
S. Sarkar,
ssarkar@geomar.de

Citation:
Sarkar, S., K. L. Sheen, D. Klaeschen, J. A. Brearley, T. A. Minshull, C. Berndt, R. W. Hobbs, and A. C. Naveira Garabato (2015), Seismic reflection imaging of mixing processes in Fram Strait, *J. Geophys. Res. Oceans*, *120*, 6884–6896, doi:10.1002/2015JC011009.

Received 10 JUN 2015
Accepted 21 SEP 2015
Accepted article online 24 SEP 2015
Published online 23 OCT 2015

Abstract The West Spitsbergen Current, which flows northward along the western Svalbard continental slope, transports warm and saline Atlantic water (AW) into the Arctic Ocean. A combined analysis of high-resolution seismic images and hydrographic sections across this current has uncovered the oceanographic processes involved in horizontal and vertical mixing of AW. At the shelf break, where a strong horizontal temperature gradient exists east of the warmest AW, isopycnal interleaving of warm AW and surrounding colder waters is observed. Strong seismic reflections characterize these interleaving features, with a negative polarity reflection arising from an interface of warm water overlying colder water. A seismic-derived sound speed image reveals the extent and lateral continuity of such interleaving layers. There is evidence of obliquely aligned internal waves emanating from the slope at 450–500 m. They follow the predicted trajectory of internal S2 tidal waves and can promote vertical mixing between Atlantic and Arctic-origin waters.

1. Introduction

Fram Strait, a 450 km wide passage located between Greenland and Svalbard, is a critical exchange point for the ocean circulation of the North Atlantic [*Hunkins*, 1990]. It is here that warm and saline Atlantic water (AW) flows into the Arctic Ocean, where it is cooled and freshened by heat loss and melting of sea ice [*Untersteiner*, 1988]. The resultant Arctic water is then exported back through Fram Strait, where it contributes significantly to the heat and freshwater budgets of the North Atlantic (Figure 1a) [*Schauer et al*., 2004]. This water mass can ultimately impact the southward-flowing limb of the North Atlantic meridional overturning circulation through its effects on ocean density, which controls the efficiency of deep convection in the Nordic Seas [*Rabe et al*., 2013].

In addition to these global impacts, warm AW within Fram Strait can influence regional ocean currents [*Beszczynska-Möller et al*., 2012a], sea ice conditions [*Kinnard et al*., 2011], nutrient and carbon transports [*Torres-Valdés et al*., 2013; *MacGilchrist et al*., 2014], the marine ecosystem [*Hunt et al*., 2013], and the stability of marine gas hydrates [*Westbrook et al*., 2009]. Heat carried by AW exerts a strong control on Arctic sea ice stability, as heat from that layer can be mixed diapycnally through its upper surface, thereby becoming available to melt ice [*Sirevaag and Fer*, 2009; *Fer et al.,* 2010b; *Polyakov et al*., 2010]. Considerable shrinkage of Arctic Ocean ice coverage in the past three decades has been linked with AW warming [*Ivanov et al*., 2012]. Moreover, increased ocean temperatures and reduced sea ice coverage encourage enhanced plankton production, which in turn influences fish populations and consequently, much of the marine ecosystem. Seasonal to decadal changes in bottom water temperature are likely to control current and future methane hydrate dissociation on the upper continental slope offshore of west Svalbard [*Marín-Moreno et al*., 2013; *Berndt et al*., 2014], triggering release of hydrate-bound methane into the ocean.

Along the continental slope of western Svalbard (Figure 1b), the northward-flowing continuation of the Norwegian Atlantic Slope Current, known as the West Spitsbergen Current (WSC), advects warm AW, reaching a depth of 450–500 m [*Orvik and Niiler*, 2002]. A layer of fresh Polar Water (PW) overlies more saline AW (Figures 1c and 1d). The PW is sourced from a combination of glacial meltwater, water from the major fjords, precipitation, and sea ice melt [*Saloranta and Svendsen*, 2001; *Cottier et al*., 2005]. The northward-flowing warm AW loses heat and salt as it mixes with the local fresh PW [*Saloranta and Svendsen*, 2001; *Sirevaag and Fer*, 2009]. The dynamics of the WSC and, in particular, the mechanisms of mixing by mesoscale processes,

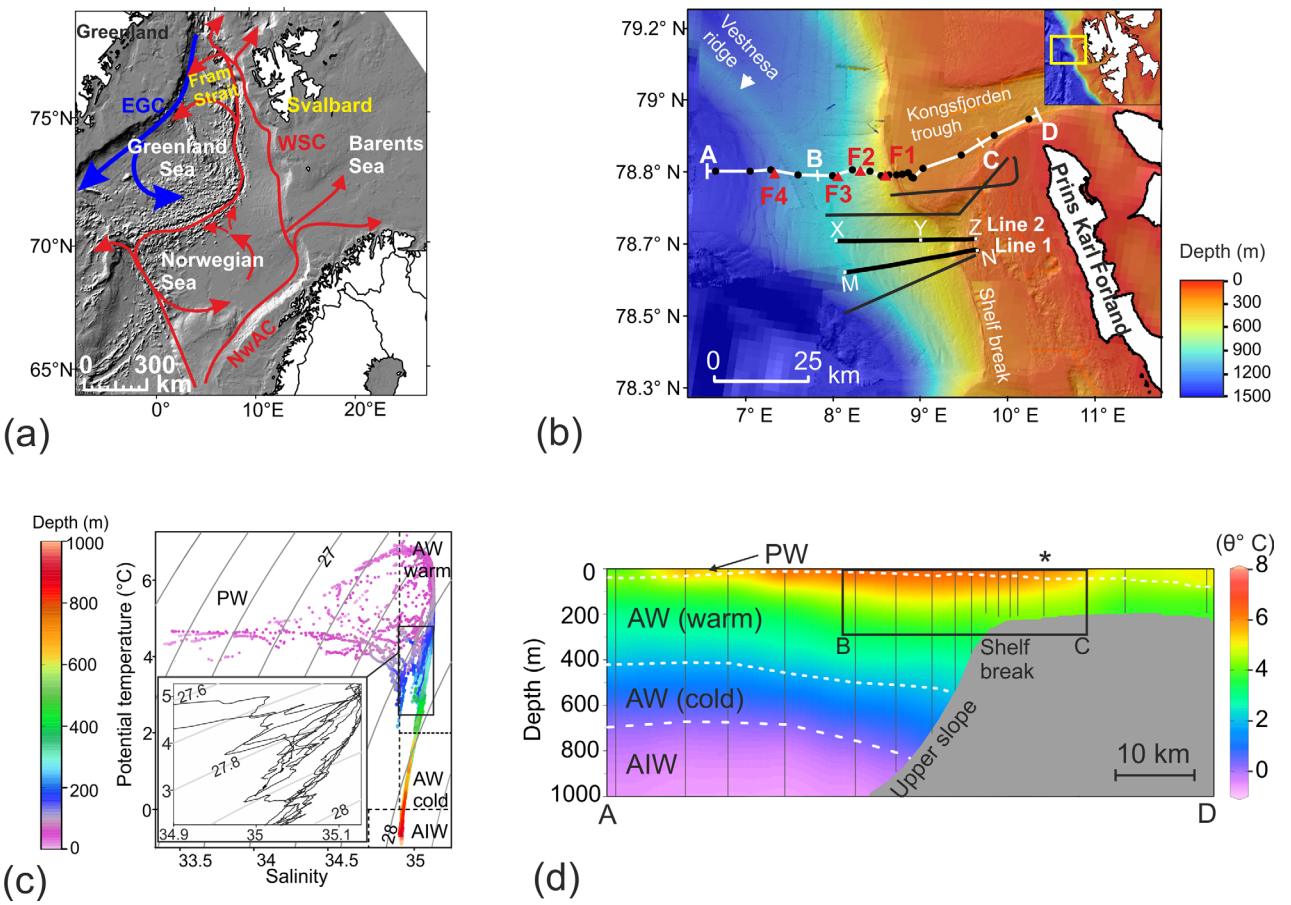

Figure 1. (a) Schematic of the circulation of the Nordic Seas, adapted from *Beszczynska-Möller et al.* [2012a]. The Norwegian Atlantic Current (NwAC, red line) is the northward-flowing eastern branch of the warm and saline Atlantic Current. The western branch of the Atlantic Current flows along the mid-oceanic ridge system. Off the coast of west Svalbard, the NwAC is known as the West Spitsbergen Current (WSC). The East Greenland Current (EGC, blue line) brings cold Arctic water from the north and flows southward along the east Greenland continental margin. (b) Locations of seismic lines (black lines) and CTD stations (black circles). The current meter mooring locations (F1–F4) are shown by red triangles. (c) Water mass divisions on the θ-S plot of the CTD data along transect AD following *Schlichtholz and Houssais* [2002]. Potential density anomaly contours in kg/m^3 (reference pressure = 0 dbar) shown in the background. PW = Polar Water, AW = Atlantic Water, and AIW = Arctic Intermediate Water. θ-S variations at the transition between PW and AW are enlarged in the inset at the lower left corner. (d) Potential temperature section along an east-west CTD transect (AD in Figure 1b) with water mass boundaries.

internal waves, and the interaction with local water masses remain sparsely investigated due to the scarce observational records both within Fram Strait and on the West Spitsbergen shelf and upper slope. Moreover, owing to their coarse lateral resolution (typically >10 km), conventional conductivity-temperature-depth (CTD) sections have considerable uncertainty in resolving the horizontal oceanic thermohaline structures associated with mixing processes. In order to improve understanding of ocean mixing and thermohaline circulation, it is important to resolve both mesoscale and fine-scale structures along hydrographic sections.

Seismic oceanography, a technique that maps acoustic reflections caused by thermohaline interfaces in the water column, provides a method of measuring oceanic thermohaline structure at unprecedented horizontal resolutions [*Ruddick et al.*, 2009]. The technique has provided new insights into a variety of ocean phenomena, such as thermohaline interleaving [*Holbrook et al.*, 2003], internal waves [*Holbrook and Fer*, 2005], double diffusive layering [*Biescas et al.*, 2008], thermohaline staircases [*Fer et al.*, 2010a] large-scale overturns [*Sheen et al.*, 2012] and mesoscale eddies [*Sheen et al.*, 2009].

In this study, we use multichannel seismic reflection data collected west of Svalbard, alongside complementary hydrographic measurements, to examine the characteristics of the local thermohaline fine structure. The main objectives of this study are (1) to map out the high-lateral-resolution spatial structure of the water mass boundaries in the region, and (2) to understand the role of mesoscale and fine-scale physical

processes in promoting both lateral and vertical mixing between warm AW and surrounding water masses. This work aims at a qualitative description of mixing processes using seismic data collected in summer 2008, concentrating on the warm AW in Fram Strait.

2. CTD, Seismic, and Ancillary Data

Conductivity-temperature-depth (CTD) data for the study area were compiled from the World Ocean database 2009 [*Boyer et al*., 2009]. Sixteen CTDs (Sea-Bird MicroCAT SBE37) covering water depths from 260 to 1500 m were collected on 12 September 2008 onboard RV Håkon Mosby (CTD transect AD in Figure 1b). The CTD spacing varied along this transect: it was ∼10 km above the shelf and shelf break, ∼3 km above the uppermost continental slope (water depths 300–800 m), and ∼7 km above much of the slope (water depths 800–1500 m). Potential temperature (θ), potential density (ρ), and sound speed (c) were derived from the CTD data following the international thermodynamic equation of seawater-2010 [*IOC et al*., 2010]. Salinity (S) presented here is unitless on the Practical Salinity Scale-1978. Our analysis uses these CTDs due to their proximity in time and space to our seismic data set.

Multichannel seismic reflection (MCS) data were collected during the cruise JR211 onboard *RRS James Clark Ross* between 5 and 7 September 2008 (Figure 1b). The seismic lines are almost perpendicular to the main flow direction of the WSC. The seismic source consisted of two generator-injector air guns, each with a volume of 2.46 L (150 cubic inches), 0.74 L (45 cubic inches) generator, and 1.72 L (105 cubic inches) injector and towed at a depth of 3 m. The air gun firing interval was 5 s (∼12.5 m) and the sampling rate was 1 ms. The seismic streamer was 600 m long with ninety-six 6.25 m long hydrophone groups. Data processing included removing the direct arrival using an eigenvector filter, common midpoint binning (bin size 3.125 m), a static shift of −9 ms (as the source wavelet does not start at zero time), band-pass filtering (Ormsby band-pass filter with corner frequencies at 10, 20, 100, and 200 Hz), a geometric spreading correction, and true amplitude prestack time migration with CTD-derived sound speed. The wavelet for the reflections in the water column shows peak energy at frequency about 70–75 Hz. Assuming a constant sound speed of 1470 m/s, the vertical resolution is ∼5 m. Sound speed was derived from the seismic data.

Multibeam swath-bathymetry of the upper continental slope was collected during the JR211 cruise (gridded to 20 m cell size) [*Sarkar et al*., 2011]. We also used current meter data to compute tidal harmonics. We analyzed Aanderaa RCM9 current meter mooring data from 7 July 2008 to 3 July 2009 to determine the tidal components on the upper continental slope of west Svalbard. Conductivity, temperature, and pressure were recorded by CTDs (Sea-Bird MicroCAT SBE37) at the moorings. Mooring locations (F1–F4) are shown in Figure 1b. *Teigen et al*. [2010] provided a detailed overview of all the moorings (F1–F7). Current meters were instrumented at depths of 70, 250, 750, and 1500 m [*Beszczynska-Möller et al*., 2012b] and sampled at intervals of 2 h. The tidal harmonic analysis was performed using the Matlab software routine T_TIDE [*Pawlowicz et al*., 2002]. We interpolated the time series of eastward (u) and northward (v) flowing current components onto an hourly time base as an input requirement for T_TIDE.

3. Water Mass Structure

A θ-S plot (Figure 1c) of the CTD data along transect AD shows that water masses of four categories are present: PW ($\theta > 0$°C; S < 34.9), two types of AW ($\theta > 2$°C, S > 34.91 (warm AW); 0°C < θ < 2°C, S > 34.91 (cold AW)), and Arctic Intermediate Water (AIW, −1.1°C < θ < 0°C; 34.7 < S < 34.9). Water mass boundaries are shown on the potential temperature section obtained from the CTDs (Figure 1d). Warm AW occurs below a thin cap of PW that is usually 10–50 m thick but thickens up to ∼150 m to the east on the shelf. The temperature and salinity records from the moorings were analyzed to understand temporal variations of the water mass structure in the 1 week gap that occurred between seismic and CTD data collection. Based on both these data sets obtained from 5 to 12 September 2008, the transition between warm and cold AW varied between 550 and 600 m and the transition between cold AW and AIW was found at 700–800 m depth. The WSC warm core carrying AW ($\theta \sim 7$°C, in September, the peak of summer) is usually found at ∼50 m below the sea surface and is confined to the upper continental slope in the west Svalbard region. The transition between PW and warm AW is marked by a saw-tooth pattern on the θ-S diagram (Figure 1c, inset) indicating interleaving of warm, salty water with colder, fresher water. Such a saw-tooth pattern is also known from the Arctic Ocean, e.g. [*Rudels et al*., 2000].

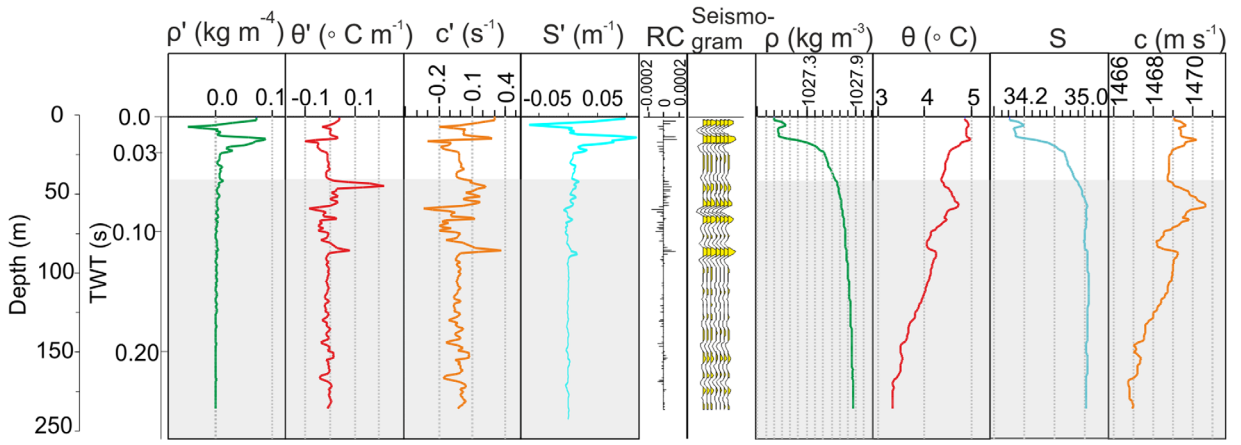

Figure 2. Vertical gradient of density (ρ'), vertical gradient of potential temperature (θ'), vertical gradient of sound speed (c′), vertical gradient of salinity (S′), reflection coefficient (RC), seismogram (generated by convolving a 75 Hz Ricker wavelet with the reflectivity series and peaks are filled by yellow color), variation of density (ρ), potential temperature (θ), salinity (S), and sound speed (c) obtained from a CTD (CTD position indicated by an asterisk in Figure 1d) in the shelf. The gray shaded region marks the field of warm Atlantic water. The reflection coefficient is strongly influenced by salinity variations in the top 35 m but the influence of temperature and sound speed variations on RC is obvious in depths >35 m. Large changes in θ' and c′ occur in conjunction with little change in ρ'.

4. Dependence of Reflectivity on Sound Speed and Temperature

Seismic reflection can be interpreted as a convolution of the source wavelet with the medium's reflection coefficient, which is determined by the acoustic impedance (sound speed × density) change [*Sheriff and Geldart*, 1995]. The latter is in turn related to the temperature and salinity change across a boundary. Based on CTD data, *Sallarès et al.* [2009] estimated that sound speed variations provide 90–95% of the seismic reflectivity, whereas only 5–10% is the result of density changes. Based on their method, we find that sound speed variations, derived from the CTD data, provide 92% of the reflectivity in the study area. Typically, seismic images of the ocean are proxies for the temperature gradient as reflectivity is more strongly correlated to temperature variations than salinity variations in the water [*Ruddick et al.*, 2009]. However, for the Arctic region, this relationship needs to be further examined because the salinity contribution to ocean stratification is considered to be significant and consequently, the relative contribution of salinity and temperature to reflectivity was ascertained. Based on CTD data, we find that in the top 50 m of the water column in the study area, the contribution of salinity to reflectivity (55–60%) dominates over temperature fluctuations (45–40%), which contrasts with a 12–18% contribution of salinity inferred elsewhere [*Sallarès et al.*, 2009]. However, in water depths between 50 and 250 m, the salinity contribution to acoustic impedance is only 12–18% and the temperature contribution (82–88%) dominates. Therefore, seismic reflections in the water depths between 50 and 250 m more likely result from fluctuations associated with temperature. We also find that temperature and sound speed variations correlate strongly (correlation coefficient 0.98). Therefore, sound speed variations derived from seismic data could be effectively used to understand relative variations in temperature. The seismic data provide band-limited information on the acoustic impedance contrast which identifies the boundaries in water column. Following *Papenberg et al.* [2010], stochastic deconvolution of time-migrated seismic data was used to derive reflection coefficients and to map out laterally coherent reflectivity caused by fine-scale ocean layering. Reflection coefficients were inverted to obtain relative sound speed perturbation. The relative sound speed was merged with the background sound speed obtained from the CTDs. We used sound speed from the CTDs because of the band-limited nature of the seismic signal (>10 Hz) that prevents us from obtaining the long vertical wavelength (>150 m) variation of the sound speed. The mean relative error in sound speed variations associated with the above analysis is ±0.1 m/s (maximum ±0.5 m/s). Additionally, we generated synthetic seismograms (an example shown in Figure 2) by convolving the seismic source wavelet with CTD-derived reflectivity series and find a strong correlation with vertical sound speed and temperature derivatives compared to those of density and salinity below 50 m, which can be seen in the vertical gradients of sound speed and temperature and the similarity between peaks. Therefore, we use the polarity of reflections as an additional criterion to understand the transition between water masses with variable temperature in seismic profiles. For example, a negative polarity reflection signifies that warm water (and therefore, higher sound speeds) overlies colder water, as a negative acoustic impedance contrast is created at such an interface.

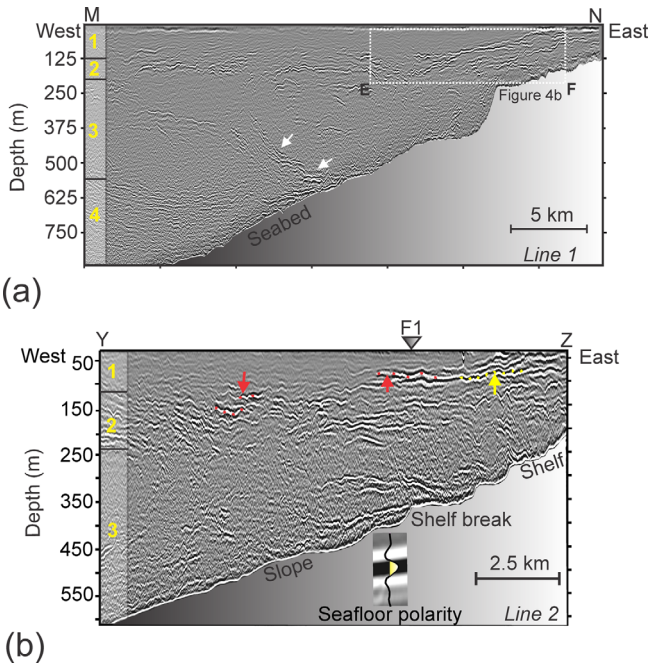

Figure 3. (a) Line 1 showing Zones 1–4. Black and white bands indicate acoustic reflections from thermohaline variability. Section EF was further analyzed for sound speed variations and shown in Figure 4. (b) Line 2 showing water column reflections above the shelf and upper slope. Zone 1, characterizing the warmest AW, thins out toward the shelf. In the top 250 m, reflections are usually long, gently undulating, and more continuous above the shelf and shelf break. Here strong negative (marked by red dots and arrows) as well as positive polarity reflections (marked by yellow dots and arrow) are observed. Above the slope and at ~150 m, reflection continuity is disrupted. The mean position of the maximum northbound WSC is ~3 km west of current meter mooring F1 [*Teigen et al.*, 2010].

5. Seismic Image Analysis

In the seismic profiles, we identify four zones (1–4) in the top 800 m of the water column based on reflection patterns (Figure 3a) and correlate these zones with the water mass structure by comparing with potential temperature and sound speed sections from CTDs. The nearest seismic line is 3 km away from the CTD transect. The seismic reflection patterns observed on all our across-slope seismic lines are similar to the seismic line nearest to the CTDs. Here we present seismic Lines 1 and 2 (Figure 1b) as they very clearly show most of the fine structures seen in the study area.

Zone 1 is a low reflectivity region (depths shallower than 125 m), which has a wedge shape and thins toward the shelf break (Figure 3a). This zone corresponds to the warmest AW ($\theta > 6$°C and mean sound speed $>$ 1476 m/s). A strong negative polarity reflection marks the base of the zone and indicates the presence of colder water immediately below the warmest AW. The shape and extent of this zone seen on several across-slope seismic lines could be matched very well with the temperature and sound speed sections obtained from the CTDs and served as a useful criterion to corroborate CTD-based sound speed and temperature sections to distant seismic lines (Figure 1b).

Zone 2 (125–250 m depth) comprises strong to moderate reflections with wavy patterns and variable reflection continuity (Figure 3a). Strong reflections interleave with regions of weaker reflections. In this zone, there exists a region of relatively high-amplitude, long, continuous, and gently undulating near-horizontal reflections in the shelf (Figure 3b). Below the band of bright reflections, we find patchy areas of weak reflectivity and few short, bright reflections. Reflections become more disrupted and discontinuous over the upper continental slope. Zone 2 coincides with a transition from the warmest AW to surrounding colder water (6°C $< \theta <$ 4°C). In this zone, sound speed (least squares regression line fitted to sound speed obtained from CTDs above the upper slope) varied linearly from 1476 m/s at 75 m to 1466 m/s at 250 m. Sound speed derived from the current meters (F2–F3) in this zone varied in a similar fashion during the time seismic data were acquired (e.g., Line 1, Figure 1b), but the absolute sound speed values were slightly higher (~0.07%) at all measured depths in the top 250 m than the mean sound speed values derived from CTDs at corresponding depths. Assuming that the sound speed structure between the CTD transect and seismic Line 1 did not vary significantly, and as the absolute mean sound speed variation in Zone 2 was minor between the time seismic Line 1 and CTD data were acquired, we derived a sound speed model by combining CTD-based sound speed (Figure 4a) and seismic reflectivity from Line 1 to understand fine-scale variations of relative sound speed in this zone (Figure 4b). The sound speed model (Figure 4c) highlights interleaving between warm (higher sound speed) and cold (slower sound speed) water bearing areas immediately below the warmest AW.

Zone 3 (250–500 m) is mostly acoustically transparent with a few distinct reflections. It corresponds to AW with θ between 3°C and 4°C and average sound speed between 1466 and 1465 m/s. Although generally transparent, obliquely dipping reflections emerge at the vicinity of the seabed (marked by white arrows in Figure 3a), which are prominent in most of the slope-perpendicular seismic lines and they help to characterize this zone.

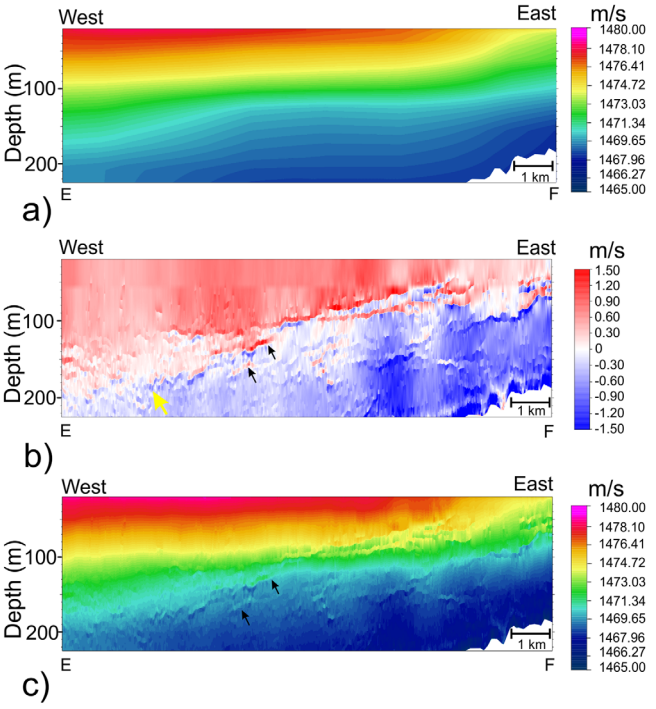

Figure 4. (a) Sound speed obtained from the CTDs shown in Figure 5a. (b) Relative sound speed perturbation obtained after applying a low-cut filter (cutoff frequency 10 Hz) to the reflection coefficients derived from the seismic data (section EF, Line 1, Figure 3a). Black arrows indicate several short, steeply dipping layers above the upper slope. At ~150 m and close to the western end of the section (yellow arrow), the continuity of the layers is disturbed. (c) Sound speed model produced after merging background (Figure 4a) and relative sound speeds (Figure 4b). In the top 100 m, warm water layers (higher sound speed) interleave with regions of relatively colder water (slower sound speed). Black arrows indicate steeply dipping interleaving layers.

Zone 4 (500 and 800 m) is the basal zone. Reflections with poor reflection continuity are found in the upper region (depths 550–650 m, Figure 3a). It corresponds to $3°C < \theta < 0°C$ and 1460 m/s < c < 1465 m/s. A few continuous reflections can be traced over long distances (>2 km). As the transition from warm AW to cold AW is found at 500–550 m depth (Figure 1d), the upper boundary of Zone 4 is likely to correspond to the boundary between these two water masses.

6. The Transition Between the Warmest AW and Surrounding Colder Waters

The mixing between warm and cold waters both on the onshore and offshore sides of the warmest AW has previously been studied using conventional hydrographic data. *Cokelet et al.* [2008] showed isopycnals pass through the warmest AW and outcrop on the offshore side of it, indicating that AW can communicate with the sea surface along the isopycnals. *Boyd and D'Asaro* [1994] suggested that mesoscale eddies diffuse heat along isopycnals to the sea surface, which will then be cooled by the atmosphere and sea ice. *Cottier and Venables* [2007] described the thermohaline characteristics to the east of the AW warm core from further south of the study area. From a hydrographic transect collected in September 2005, they proposed double diffusion to be a likely process in the Arctic frontal region with considerable interleaving west of Isfjorden Bank. Double diffusion takes place due to a difference in the diffusivities for heat and salt with the molecular diffusivity of heat being approximately 100 times larger than that of salt [*Ruddick and Richards*, 2003]. Double-diffusion can result in a variety of phenomena, namely salt fingering and diffusive convection that can break a smoothly varying thermohaline gradient into steps and layers. In the Kongsfjorden trough region, a large horizontal temperature gradient is seen shelfward of the warmest AW on the upper continental slope (Figure 5a). A salinity front coincident with the temperature front is situated near the shelf break and below the PW cap (Figure 5b). Layers of saline water extend horizontally from the salinity front further east onto the shelf. Both the potential temperature and salinity sections reveal interleaving of warm, salty water and colder, fresher water (Figures 5a and 5b) that can enhance double-diffusive mixing in the frontal region. We computed Turner angle values [*Ruddick*, 1983], which indicate the potential for diffusive layering at the interface of interleaving warm, salty water with colder, fresher water (Figure 5c). Much of Zone 2 on the upper slope is susceptible to salt fingering, suggesting that the shelf break and upper slope regions may be influenced by this process. On the shelf, we find sites susceptible to diffusive convection and salt fingering at the top and bottom of the warm and salty water layer, respectively, occurring within colder, fresher water. At the transition between the warm, salty water layers and the colder, fresher water layers, relatively high Turner angle values (±70°–78°) indicate that the density effect of temperature variation is partially neutralized by the density effect of salinity variation and partial density compensation is achieved.

The seismic data and the derived sound speed structure (Figure 4c) from the onshore side of the warmest AW reveal salient details of the transition between warm AW and colder water on the shelf. Sound speed variation is

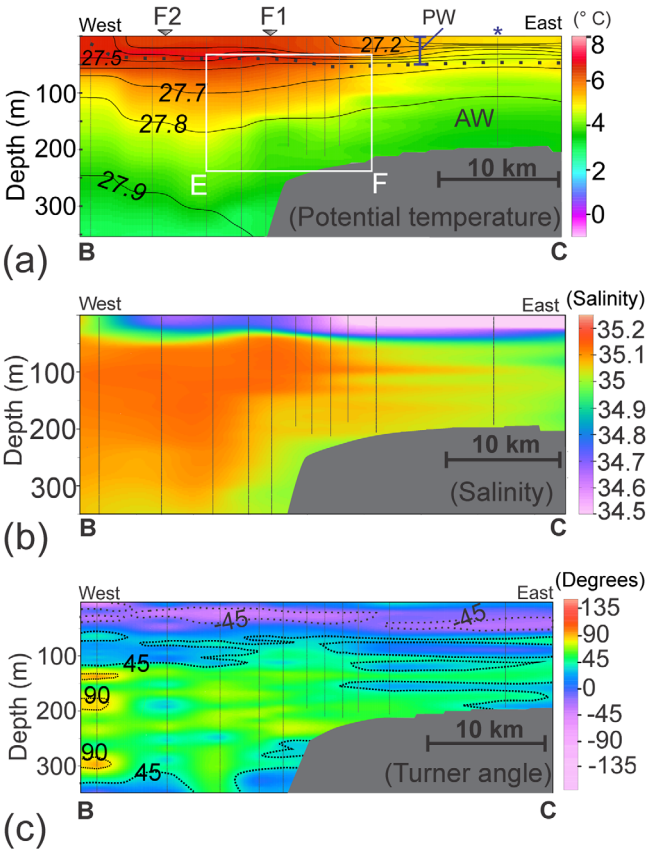

Figure 5. (a) A potential temperature section (BC, location in Figure 1d) along with potential density anomaly contours in kg/m^3 (overlaid). A CTD (indicated by an asterisk and shown in Figure 2) reveals temperature variations that are partially density compensated by salinity variations. A background sound speed model (Figure 4a) is derived from the region marked by a white rectangular box. (b) A salinity section (BC, location in Figure 1d) showing the presence of a horizontal salinity gradient near the shelf break. (c) Section BC showing variations of Turner angles (Tu). For $-45° < Tu < 45°$, the water column is stable, whereas for $|Tu| > -90°$, the column is statically unstable. In the range $-90° < Tu < -45°$, the water column is unstable to double diffusive convection, and between $45° < Tu < 90°$, it is prone to salt fingering. Salt fingering is the predominant diffusive mechanism in the upper slope.

expected to resemble the temperature variation because sound speed gradient is closely proportional (correlation coefficient 0.98) to temperature gradient. The warmest AW has relative absence of fine structure, but prominent fine structures occur immediately below it. Filaments (~30 m thick, Figure 4c) of higher sound speed (therefore, warmer water) interleave with areas of lower sound speed (therefore, colder water) at water depths 50–150 m. Above the shelf break, we find near-horizontal, long (approximately 5 km) interleaving layers and their slope (slope 0.0025–0.003) matching with along-front slope of the isopycnals (0.003) seen on the hydrographic profile. In the potential temperature section (Figure 5a), a warm interleaving layer at ~75 m depth over the shelf closely follows the 27.7 kg/m^3 potential density anomaly contour, indicating isopycnal interleaving. This observation is also in agreement with previously reported isopycnal interleaving found above the shelf by *Cottier and Venables* [2007]. A limited number of interleaving layers above the uppermost continental slope have steeper slope (slope 0.02–0.03 and marked by black arrows in Figures 4b and 4c), therefore, crossing the isopycnals (isopycnal slope 0.0025). The lateral continuity of the interleaving layers deteriorates with increasing depth, for example, water depths150–200 m, where the reflectors are shorter (e.g., 500 m).

The formation of interleaving layers, disruption of their continuity, and variations in their slope can be understood by considering the dynamics of the warm Atlantic water. The warm core of WSC flows faster than the shelf waters and introduces a strong horizontal velocity shear [*Teigen et al.*, 2010]. According to *Nilsen et al.* [2006], the shear associated with a Gaussian current jet carrying a warm AW core can produce unstable eddies. Such a jet is located between current meter mooring stations F1 and F3 [*Teigen et al.*, 2010, Figure 1]. The mean position of the maximum northbound WSC is halfway between current meter moorings F1 and F2 [*Teigen et al.*, 2010]. Stronger internal waves in regions with strong currents can destroy the lateral coherence of thermohaline fine structures. This effect is seen in the upper slope region in Zone 2 where the lateral continuity of the reflections is disturbed (Figures 3b and 4b). *Steele et al.* [2012] found high turbulent kinetic energy dissipation rates to the east of the warmest AW (e.g., their Figures 3d and 3f) and suggested this could be due to presence of eddies of variable sizes, such as less than 500 m diameter and also ~1 km in diameter. The limited number of isopycnal-crossing interleaving layers on the uppermost continental slope would require the presence of an eddy close to that region. The scenario could be very similar to observations made by *Smith and Ferrari* [2009], who suggested that eddies can act on large-scale thermohaline gradients to produce sharp fronts that are tilted by mesoscale vertical shear. Such a process can locally enhance temperature and sound speed gradients and accentuate the interfaces between warm and cold waters, which are imaged very well by the seismic data. The regions with poor reflectivity could indicate

homogenous water masses that result from mixing. To the east of this region and above the shelf, isopycnal interleaving layers (Figure 5a) indicate partially density-compensated gradients in temperature (therefore, sound speed, Figure 2) and salinity allowing for stirring along isopycnals. We propose that here the interleaving features are most likely to arise from mesoscale eddy stirring of the large-scale distribution of thermohaline properties along isopycnal surfaces, e.g. [*Naveira Garabato et al*., 2011].

A diffusive mechanism can also set smoothly varying temperature and salinity gradients into steps, however, eddies/frontal instability is more important in this region in setting up the interleaving layers as opposed to double diffusion, which takes place in low-energy environment. Although double-diffusive transport does not appear to be the main causative factor behind interleaving, it could still play a role once interleaving has been established. Seismic profiles reveal the presence of undulations in the reflections from the frontal region, which indicate the presence of internal waves generated by turbulence. Earlier, *Saloranta and Haugan* [2004] emphasized the role of diapycnal mixing processes in addition to isopycnal cooling for subsurface cooling offshore from the warm AW core. Turbulent mixing (for example, stirring by an eddy field) can also aid diapycnal mixing across density surfaces [*Thorpe*, 2005] and will enhance vertical heat and salt fluxes. While conventional CTD data could only indicate a strong lateral temperature and sound speed gradient to the east of the warmest AW, the detailed frontal structure to the east of warmest AW including the lateral extent and nature of interleaving layers revealed by the seismic images helped to understand the causative factor behind their formation, such as the role of eddy stirring in enhancing the θ/c gradients and distributing large-scale variations in temperature and salinity.

7. Internal Tidal Waves

Oblique reflections in across-slope profiles occur near the seafloor at depths of ~450–500 m (Figure 6a). Where present, they stand out clearly in Zone 3. Similar reflections were reported earlier by *Holbrook et al*. [2009] from the Norwegian continental slope (64°N–66°N). They interpreted the sloping reflections, which cross isotherms, as internal waves propagating at tidal frequencies. In their case, the internal waves closely followed the trajectory of semidiurnal (M2) internal tidal waves. The sloping reflections observed west of Svalbard appear to be very similar. When surface (barotropic) tides force stratified fluids to flow over sloping topography, internal baroclinic tides are generated that can emanate as internal tidal beams from the slope [*Holloway and Merrifield*, 1999; *Garrett and Kunze*, 2007]. Such beams can cause substantial vertical displacement of isopycnals in the ocean interior and also trigger internal waves that propagate away from their generation site along the trajectory of the internal tidal wave. Seismic reflections can result from the strain of the potential density field [*Thorpe*, 2005] induced by an internal wave field [*Holbrook et al*., 2009]. The frequency of such internal waves remains close to the frequency of the barotropic surface tide that triggers internal tidal waves [*Thorpe*, 2005].

The two major semidiurnal tides observed from the recorded measurements at various locations in the Arctic Ocean are M2 (principal lunar) and S2 (principal solar) [*Kowalik and Proshutinsky*, 1994]. Propagation of internal tidal waves is usually determined by the relative magnitudes of three frequencies: the internal wave frequencies ω of the semidiurnal tides ($\omega_{S2} = 1.454 \times 10^{-4}$ s^{-1}, $\omega_{M2} = 1.405 \times 10^{-4}$ s^{-1}), the local buoyancy frequency $N(z) = [-(g/\rho)\partial\rho/\partial z]^{1/2}$ (where g is the acceleration of gravity and ρ is the potential density, Figure 6b), and the local inertial (Coriolis) frequency, $f = 1.423 \times 10^{-4}$ s^{-1} at 78°N. The inclination of the tidal wave is given by $c = \tan\theta = [(\omega^2 - f^2)/(N^2 - \omega^2)]^{1/2}$. In previous studies, these tidal processes were only theoretically considered and their probable sites of generation determined based on a coarse-resolution bathymetric data set [Figure 4 of *Naveira Garabato et al*., 2004]. Modeling results by *Müller* [2013] suggested that barotropic to baroclinic tidal energy conversion is highest for M2 and negligible for S2 over the entire Arctic region. He proposed that poleward of the critical latitude the energy conversion associated with the semidiurnal tides is insignificant.

West of Svalbard, the principal semidiurnal tide M2 remains subinertial and cannot usually generate internal tidal waves as $\omega_{M2} < f$, hence the Coriolis force will suppress M2 internal waves. However, they can exist under the influence of negative background vorticity, which weakens the local Coriolis force [*Vlasenko et al*., 2003]. Analysis of along-slope and across-slope components of current velocity during our seismic survey from three current meters on the upper slope (F1, F2, and F3) shows a persistent anticyclonic motion landward of station F2 at the level of 250 m that introduces a negative background vorticity (mean $= -3.85 \times 10^{-6} \pm 0.83$ s^{-1}, minimum $= -5.15 \times 10^{-6}$ s^{-1}, maximum $= -2.75 \times 10^{-6}$ s^{-1}), which results in a suppressed effective inertial frequency (measured as 1.423×10^{-4} s^{-1} + 0.5 × relative vorticity) of at least 1.40×10^{-4} s^{-1}. Based on rotary

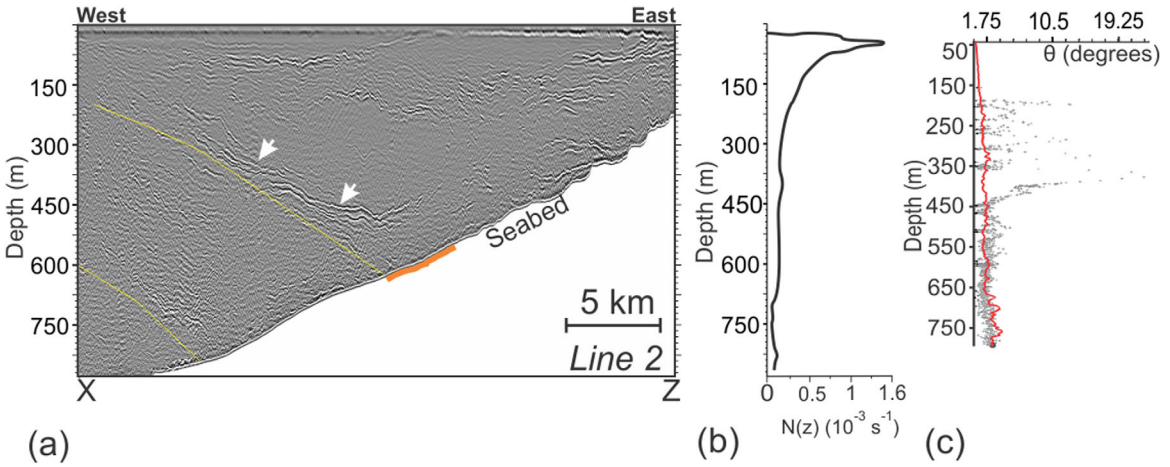

Figure 6. (a) Seismic Line 2 showing dipping reflections (marked by white arrows) over a broad area of the slope (450–500 m). They follow the S2 internal tidal wave trajectory (yellow line). Close to the seabed (at ~550 m and highlighted by an orange stripe), the fine structures associated with internal waves grade into a transparent zone and may indicate wave breaking and subsequent mixing as a homogenous water mass develops. (b) Mean buoyancy frequency N (z) determined by CTDs shown in Figure 1b. (c) Ray slope of internal S2 tidal wave (red curve) and seafloor slope (gray crosses) derived from multibeam swath-bathymetric data close to Line 2. Between 450 and 750 m they are very similar.

spectral analysis, *Nilsen et al.* [2006] showed that the energy levels for the M2 component are higher landward of F2, and that there is elevated energy in the anticyclonic rotation component. Despite the likely presence of an M2 tidal current at this depth, the inclined reflection in the seismic image is not consistent with a possible M2 internal tidal beam as its internal wave frequency still remains close to the Coriolis frequency. In contrast, internal S2 tidal waves can be generated as $f < \omega_{S2}$. Strong internal tidal waves can be expected where the seafloor slope γ is near critical for S2 [*Cacchione et al.*, 2002]. The γ and c variations in the vicinity of Line 2 indicate that much of the slope (derived from high-resolution swath-bathymetric data) remains critical to an S2 tidal beam in water depths of ~450–750 m (Figure 6c). The inclined reflections closely mimic the predicted trajectory of internal semidiurnal tide S2 (Figure 6a). Current meter mooring data show that they crosscut isotherms (Figure 7a). Additionally, an anticyclonic eddy causing prominent shoaling of the isotherms was seen close to current meter F4 during our seismic survey (Figure 7b), but it was located further offshore of where inclined

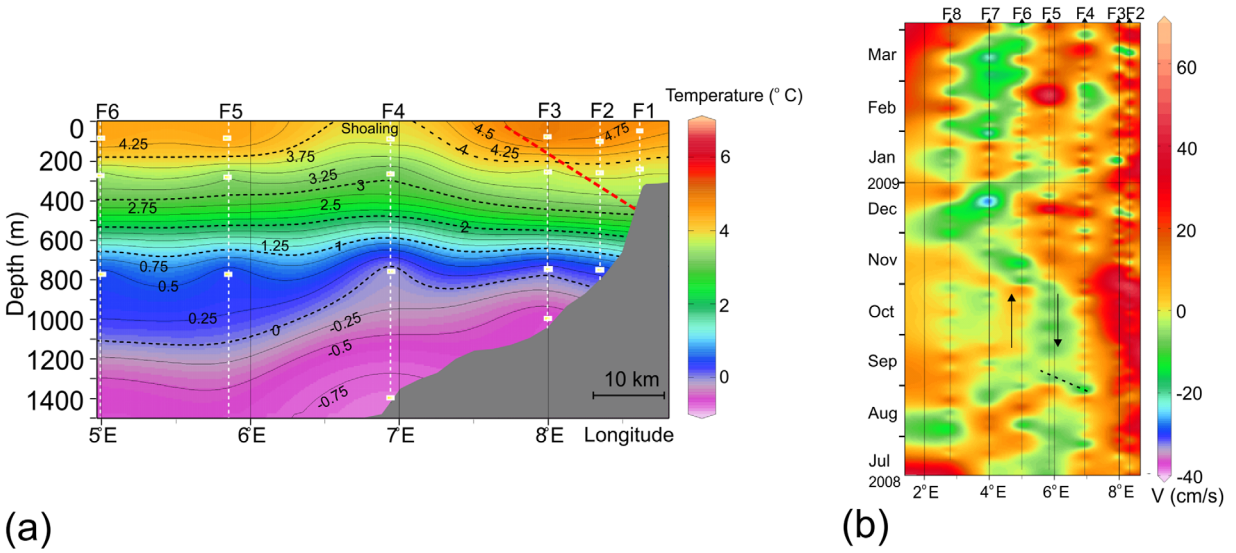

Figure 7. (a) Temperature section derived from current meters (marked by small white rectangular boxes) located at stations F1–F6. A series of temperature sections was generated from the current meters during the time seismic data were acquired (5 September 2008) but only one such section is shown. Dotted red line on the upper slope, that crosscuts isotherm, denotes location of sloping reflections seen in seismic Line 2. Similar crosscutting relationship is seen in other temperature sections obtained from the current meter data. Isotherms shoal near the shallowest current meter at station F4, which is located offshore of the region showing inclined reflections. Such shoaling is a consequence of an anticyclonic eddy passing near current meter F4. (b) Hovmöller diagram of the northbound component of current velocity at the 250 m level for moorings F2–F8 during the period July 2008 to March 2009. An anticlyclonic eddy (shown by arrows) nucleates close to F4 end of August 2008 and meanders (dotted line) westward to F5.

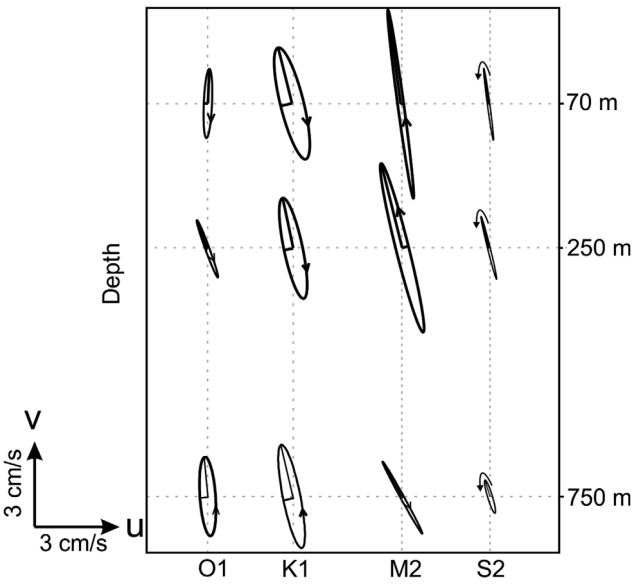

Figure 8. Tidal ellipses for the dominant diurnal constituents (O1 and K1) and semidiurnal constituents (M2 and S2) from current meter F2 at specific depths displayed on the right of the plot. The major and minor axes are plotted and sense of rotation of the ellipses is indicated by arrows.

reflections were observed (Figure 7a). We infer that these reflections do not represent upwelling caused by eddies, but that an internal S2 tidal beam exists in this area.

Previously, the presence of a strong baroclinic M2 tide in Fram Strait was only shown in regions with more than 1000 m water depth [*Kasajima and Svendsen*, 2002]. The current meter mooring station F2 (Figure 7a) located at a much shallower depth is well suited to analyze the influence of diurnal and semidiurnal tides on generating internal tides on the upper continental slope, as the station is close to the location where inclined reflections in the seismic image originate (450–500 m water depth). Tidal harmonic analysis shows that much of the shallow water column (top 250 m) at this station has flat, high-amplitude, and highly inclined ellipses for the M2 tide (Figure 8). The tidal ellipse results are summarized in Table 1. S2 ellipses are also flat but show smaller amplitudes compared to M2. Presently, there is no current meter installed where the inclined reflections originate, so we cannot comment on the tidal current pattern at this depth. However, flatter tidal ellipse patterns suggest presence of both M2 and S2 baroclinic tidal currents at the ~250 m level on the upper continental slope.

The mean slope of the inclined reflections at water depths of 150–300 m in Zone 3 is 1.12° and the theoretically computed S2 slope is 1.15°, whereas at depths of 300–550 m, the mean measured slope of reflections

Table 1. Tidal Ellipse Analysis Results for the Dominant Diurnal Constituents (O1 and K1) and Semidiurnal Constituents (M2 and S2) From Current Meter F2[a]

		Ellipse Parameters With 95% Confidence Interval (CI) Estimates								
Tide	Freq	Major	Emaj	Minor	Emin	Inc	Einc	Pha	Epha	Snr
Current Meter at 70 m Level										
O1	0.03873	1.157	0.372	0.137	0.38	87.56	16.82	153.05	16.54	9.7
K1	0.04178	1.958	0.372	0.393	0.38	103.77	10.85	233.38	10.7	28
M2	0.08051	3.35	0.212	−0.107	0.19	97.68	3.26	32.5	3.72	250
S2	0.08333	1.278	0.212	−0.043	0.19	97.58	8.32	80.31	9.5	36
Total variance = 353.7707 Predicted var =46.5139										
Percent total var predicted = 13.1%										
Current Meter at 250 m Level										
O1	0.03873	1.08	0.299	0.072	0.29	110.05	13.45	181.65	14.06	13
K1	0.04178	1.817	0.3	0.33	0.28	101.81	8.74	246.33	9.19	37
M2	0.08051	3.064	0.17	−0.227	0.15	103.95	2.88	64.14	3.27	330
S2	0.08333	1.111	0.17	−0.046	0.15	103.82	7.7	124.48	8.75	43
Total variance = 241.1222 Predicted var =37.1458										
Percent total var predicted = 15.4%										
Current Meter at 750 m Level										
O1	0.03873	1.382	0.581	−0.272	0.29	94.02	12.01	31.95	22.18	5.7
K1	0.04178	1.874	0.574	−0.311	0.31	101.21	9.39	68.21	16.74	11
M2	0.08051	1.482	0.239	0.063	0.18	118.79	7.22	48.81	9.5	38
S2	0.08333	0.65	0.253	−0.09	0.16	106.72	14.87	76.85	22.78	6.6
Total variance = 122.1358 Predicted var = 9.6556										
Percent total var predicted = 7.9%										

[a]Abbreviations: Major = Major axis amplitude (cm/s), Emaj = Error associated with Major, Minor = Minor axis amplitude, Emin = Error associated with Minor, Inc = Inclination, Pha = Phase, and Snr = Signal-to-noise ratio.

is 1.70° and the computed S2 slope is 1.75°. The change in the computed slope close to 300 m depth occurs because of a small change in local buoyancy frequency (Figure 6b). Because of the good match between calculated S2 slopes and the slope of the reflections and the location of the observed seismic reflections, we suggest that the inclined reflections in the seismic data are primarily caused by the S2 internal tide, rather than the M2 internal tide. This can be explained by the ability of S2 to cause greater strain than M2 because of its high frequency. Generally, the closer an internal wave frequency is to the buoyancy frequency, the more strain and less vertical shear the internal wave will possess [*Polzin et al*., 2014, and references therein]. Conversely, the closer an internal wave frequency is to the Coriolis frequency, the more vertical shear and less strain the internal wave will have. Thus, while the current meters show a stronger M2 than S2 tide because they measure velocity (which may or may not have vertical shear), the seismic data are more likely to exhibit an S2 signature as they are sensitive to strain. The strain [*Thorpe*, 2005] can create reversible fine structure as a result of stretching and thinning of isopycnals causing seismic reflections. The inclination of the reflections mark the trajectory of the internal wave beams [*Holbrook et al*., 2009].

In contrast to modeling results [e.g., *Müller*, 2013], our data show that semidiurnal internal tidal waves are present in Fram Strait in water depths $<$1000 m. Our current meter results also indicate that the M2 internal tide can propagate north of its nominal critical latitude (74.5°N) because of relative vorticity changes; however, such effects will be localized and evanescent. The S2 internal tide can freely propagate and an S2 tidal beam might be able to cause the strain that is observed in the seismic images.

8. Conclusions

We have obtained new high-lateral-resolution images of thermohaline fine structures from a number of seismic lines west of Svalbard. Strong seismic reflections are seen where large lateral temperature gradients occur shelfward of the warmest AW on the upper continental slope. Here we find isopycnal interleaving between warm and salty water and colder, fresher water mostly above the shelf and few steeply dipping interleaving layers above the uppermost slope and close to the warmest core. Strong reflections with both normal and reversed polarities characterize this region. Such interleaving and subsequent mixing promotes cooling of AW. While we have highlighted mesoscale eddy stirring and double diffusive phenomena as possible drivers, other dynamical processes responsible for interleaving, such as tidal mixing, remain to be determined.

Seismic images help to identify areas of internal wave generation. Sloping internal waves, which can promote ocean mixing across isopycnals, are seen close to the critical slope for S2 wave generation (450–500 m). We suggest that combined analysis of simultaneously acquired seismic data, current profiles (such as towed or vessel-mounted Acoustic Doppler Current Profiler (ADCP) data), and microstructure data would provide quantitative information on the distribution and mixing associated with internal tidal waves. Seismic data could be useful to detect areas prone to M2 internal tidal wave generation poleward of the critical latitude.

Our findings have implications for understanding the fate of AW as it mixes with cold and freshwater masses formed in the vicinity of the West Spitsbergen shelf. Lateral transfer of heat (and salt) from the warmest AW is likely to be an important process driving regional water mass modification. Additionally, the likely enhanced vertical mixing [e.g., *Rippeth et al*., 2015] promoted by internal tides, as identified in this study, will enhance the vertical fluxes of both heat and salt, which in turn may have a feedback effect on rates of sea ice formation/melting [*Holloway and Proshutinsky*, 2007].

Recent developments in oceanography have highlighted the importance of small-scale mixing for a number of physical oceanographic processes. The affected processes relevant to this study include the heat budget of the Arctic, deep water formation in the North Atlantic, and the operation of a number of important biogeochemical cycles. Recent rapid summer sea ice contraction in the Arctic and widespread atmospheric warming in the region bring into sharp focus the necessity of acquiring a systematic understanding of the interaction between warm and cold water masses on polar ocean shelves in both hemispheres, as these locations form key areas from which the deep ocean is ventilated. Our results illustrate the potential of seismic data to open up new avenues of oceanographic research in the Arctic, particularly in understanding the role of mesoscale and submesoscale processes in impacting larger-scale circulation.

Acknowledgments
This work was supported by the Natural Environment Research Council (NERC) as a part of the International Polar Year 2007–2008 (grant NE/E007058/1). The captain and crew of *RRS James Clark Ross* provided essential support for the acquisition of the data during the JR211 cruise. We thank Graham Westbrook for his leadership of the cruise and Per Trinhammer (Aarhus University) for supporting the seismic equipment. Part of the bathymetric image shown in Figure 1b was derived from the data provided by the Norwegian Hydrographic Service (NHS). S.S. is grateful to the Inlaks Shivdasani Foundation, India, the Graduate School of the National Oceanography Centre Southampton, UK, and the German Academic Exchange Service (DAAD) for financial support. K.L.S. and J.A.B. were supported by NERC. Original seismic and swath-bathymetric data from cruise JR211 are archived at the British Oceanographic Data Centre, Liverpool, and can be obtained from www.bodc.ac.uk by contacting enquiries@bodc.ac.uk. CTD data used in this study can be obtained by carrying out an online search of the database kept at www.nodc.noaa.gov/OC5/SELECT/dbsearch/dbsearch.html. Current meter mooring data can be obtained from www.pangaea.de. S.S. thanks Ilker Fer and Laurence Padman for valuable discussions. We thank four anonymous reviewers for their detailed and helpful comments.

References

Berndt, C., et al. (2014), Temporal constraints on hydrate-controlled methane seepage off Svalbard, *Science*, *343*(6168), 284–287, doi:10.1126/science.1246298.

Beszczynska-Möller, A., E. Fahrbach, U. Schauer, and E. Hansen (2012a), Variability in Atlantic water temperature and transport at the entrance to the Arctic Ocean, 1997–2010, *ICES J. Mar. Sci.*, *69*(5), 852–863, doi:10.1093/icesjms/fss056.

Beszczynska-Möller, A., E. Fahrbach, G. Rohardt, and U. Schauer (2012b), *Physical Oceanography and Current Meter Data From Mooring F1-13*, Alfred Wegener Inst., Helmholtz Cent. for Polar and Mar. Res., Bremerhaven, Germany, doi:10.1594/PANGAEA.800328.

Biescas, B., V. Sallarès, J. L. Pelegrí, F. Machín, R. Carbonell, G. Buffett, J. J. Dañobeitia, and A. Calahorrano (2008), Imaging meddy finestructure using multichannel seismic reflection data, *Geophys. Res. Lett.*, *35*, L11609, doi:10.1029/2008GL033971.

Boyd, T. J., and E. A. D'Asaro (1994), Cooling of the West Spitsbergen Current: Wintertime observations west of Svalbard, *J. Geophys. Res.*, *99*(C11), 22,597–22,618, doi:10.1029/94JC01824.

Boyer, T. P., et al. (2009), *World Ocean Database 2009*, U.S. Gov. Print. Off., Washington, D. C.

Cacchione, D. A., L. F. Pratson, and A. S. Ogston (2002), The shaping of continental slopes by internal tides, *Science*, *296*(5568), 724–727, doi:10.1126/science.1069803.

Cokelet, E. D., N. Tervalon, and J. G. Bellingham (2008), Hydrography of the West Spitsbergen Current, Svalbard Branch: Autumn 2001, *J. Geophys. Res.*, *113*, C01006, doi:10.1029/2007JC004150.

Cottier, F., V. Tverberg, M. Inall, H. Svendsen, F. Nilsen, and C. Griffiths (2005), Water mass modification in an Arctic fjord through cross-shelf exchange: The seasonal hydrography of Kongsfjorden, Svalbard, *J. Geophys. Res.*, *110*, C12005, doi:10.1029/2004JC002757.

Cottier, F. R., and E. J. Venables (2007), On the double-diffusive and cabbeling environment of the Arctic Front, West Spitsbergen, *Polar Res.*, *26*, 152–159, doi:10.1111/j.1751-8369.2007.00024.x.

Fer, I., P. Nandi, W. S. Holbrook, R. W. Schmitt, and P. Páramo (2010a), Seismic imaging of a thermohaline staircase in the western tropical North Atlantic, *Ocean Sci.*, *6*, 621–631, doi:10.5194/os-6-621-2010.

Fer, I., S. Ragnheid, and G. Florian (2010b), Internal waves and mixing in the marginal ice zone near the Yermak Plateau, *J. Phys. Oceanogr.*, *40*, 1613–1630, doi:10.1175/2010JPO4371.1.

Garrett, C., and E. Kunze (2007), Internal tide generation in the deep ocean, *Annu. Rev. Fluid Mech.*, *39*, 57–87, doi:10.1146/annurev.fluid.39.050905.110227.

Holbrook, W. S., and I. Fer (2005), Ocean internal wave spectra inferred from seismic reflection transects, *Geophys. Res. Lett.*, *32*, L15604, doi:10.1029/2005GL023733.

Holbrook, W. S., P. Paramo, S. Pearse, and R. W. Schmitt (2003), Thermohaline fine structure in an oceanographic front from seismic reflection profiling, *Science*, *301*(5634), 821–824, doi:10.1126/science.1085116.

Holbrook, W. S., I. Fer, and R. W. Schmitt (2009), Images of internal tides near the Norwegian continental slope, *Geophys. Res. Lett.*, *36*, L00D10, doi:10.1029/2009GL038909.

Holloway, G., and A. Proshutinsky (2007), Role of tides in Arctic ocean/ice climate, *J. Geophys. Res.*, *112*, C04S06, doi:10.1029/2006JC003643.

Holloway, P. E., and M. A. Merrifield (1999), Internal tide generation by seamounts, ridges, and islands, *J. Geophys. Res.*, *104*(C11), 25,937–25,951, doi:10.1029/1999JC900207.

Hunkins, K. (1990), A review of the physical oceanography of Fram Strait, in *The Physical Oceanography of Sea Straits*, edited by L. J. Pratt, pp. 61–93, Springer, Amsterdam.

Hunt, G. L., Jr., et al. (2013), The Barents and Chukchi Seas: Comparison of two Arctic shelf ecosystems, J. *Mar. Syst.*, *109*, 43–68, doi:10.1016/j.jmarsys.2012.08.003.

IOC, SCOR, and IAPSO (2010), *The International Thermodynamic Equation of Seawater—2010: Calculation and Use of Thermodynamic Properties, Intergovernmental Oceanographic Commission, Manuals and Guides No. 56*, 196 pp., UNESCO, Southampton, U. K.

Ivanov, V. V., V. A. Alexeev, I. Repina, N. V. Koldunov, and A. Smirnov (2012), Tracing Atlantic water signature in the Arctic sea ice cover east of Svalbard, *Adv. Meteorol.*, *2012*, 11, doi:10.1155/2012/201818.

Kasajima, Y., and H. Svendsen (2002), Tidal features in the Fram Strait, *Cont. Shelf Res.*, *22*, 2461–2477, doi:10.1016/S0278-4343(02)00132-2.

Kinnard, C., C. M. Zdanowicz, D. A. Fisher, E. Isaksson, A. de Vernal, and L. G. Thompson (2011), Reconstructed changes in Arctic sea ice over the past 1,450 years, *Nature*, *479*(7374), 509–512, doi:10.1038/nature10581.

Kowalik, Z., and A. Yu. Proshutinsky (1994), The Arctic Ocean tides, in *The Polar Oceans and Their Role in Shaping the Global Environment*, pp. 137–158, AGU, Washington, D. C.

MacGilchrist, G. A., A. C. N. Garabato, T. Tsubouchi, S. Bacon, S. Torres-Valdes, and K. Azetsu-Scott (2014), The Arctic Ocean carbon sink, *Deep Sea Res., Part I*, *86*, 39–55, doi:10.1016/j.dsr.2014.01.002.

Marín-Moreno, H., T. A. Minshull, G. K. Westbrook, B. Sinha, and S. Sarkar (2013), The response of methane hydrate beneath the seabed offshore Svalbard to ocean warming during the next three centuries, *Geophys. Res. Lett.*, *40*, 5159–5163, doi:10.1002/grl.50985.

Müller, M. (2013), On the space- and time-dependence of barotropic-to-baroclinic tidal energy conversion, *Ocean Modell.*, *72*, 242–252, doi:10.1016/j.ocemod.2013.09.00.

Naveira Garabato, A. C., K. I. C. Oliver, A. J. Watson, and M.-J. Messias (2004), Turbulent diapycnal mixing in the Nordic seas, *J. Geophys. Res.*, *109*, C12010, doi:10.1029/2004JC002411.

Naveira Garabato, A. C., R. Ferrari, and K. L. Polzin (2011), Eddy stirring in the Southern Ocean, *J. Geophys. Res.*, *116*, C09019, doi:10.1029/2010JC006818.

Nilsen, F., B. Gjevik, and U. Schauer (2006), Cooling of the West Spitsbergen Current: Isopycnal diffusion by topographic vorticity waves, *J. Geophys. Res.*, *111*, C08012, doi:10.1029/2005JC002991.

Orvik, K. A., and P. Niiler (2002), Major pathways of Atlantic water in the northern North Atlantic and Nordic Seas toward Arctic, *Geophys. Res. Lett.*, *29*(19), 1896, doi:10.1029/2002GL015002.

Papenberg, C., D. Klaeschen, G. Krahmann, and R. W. Hobbs (2010), Ocean temperature and salinity inverted from combined hydrographic and seismic data, *Geophys. Res. Lett.*, *37*, L04601, doi:10.1029/2009GL042115.

Pawlowicz, R., B. Beardsley, and S. Lentz (2002), Classical tidal harmonic analysis including error estimates in MATLAB using T_TIDE, *Comput. Geosci.*, *28*, 929–937, doi:10.1016/S0098-3004(02)00013-4.

Polyakov, I. V., et al. (2010), Arctic Ocean warming contributes to reduced polar ice cap, *J. Phys. Oceanogr.*, *40*, 2743–2756, doi:10.1175/2010JPO4339.1.

Polzin, K. L., A. C. N. Garabato, T. N. Huussen, B. M. Sloyan, and S. Waterman (2014), Finescale parameterizations of turbulent dissipation, *J. Geophys. Res. Oceans*, *119*, 1383–1419, doi:10.1002/2013JC008979.

Rabe, B., P. A. Dodd, E. Hansen, E. Falck, U. Schauer, A. Mackensen, A. Beszczynska-Moeller, G. Kattner, E. J. Rohling, and K. Cox (2013), Liquid export of Arctic freshwater components through the Fram Strait 1998-2011, *Ocean Sci.*, *9*(1), 91–109, doi:10.5194/os-9-91-2013.

Rippeth, T. P., B. J. Lincoln, Y.-D. Lenn, J. A. M. Green, A. Sundfjord, and S. Bacon (2015), Tide-mediated warming of Arctic halocline by Atlantic heat fluxes over rough topography, *Nat. Geosci.*, *8*(3), 191–194, doi:10.1038/ngeo2350.

Ruddick, B. (1983), A practical indicator of the stability of the water column to double-diffusive activity, *Deep Sea Res., Part A*, *30*(10), 1105–1107, doi:10.1016/0198-0149(83)90063-8.

Ruddick, B., and K. Richards (2003), Oceanic thermohaline intrusions: Observations, *Prog. Oceanogr.*, *56*(3–4), 499–527, doi:10.1016/S0079-6611(03)00028-4.

Ruddick, B., H. Song, C. Dong, and L. Pinheiro (2009), Water column seismic images as maps of temperature gradient, *Oceanography*, *22*(1), 192–205, doi:10.5670/oceanog.2009.19.

Rudels, B., R. Meyer, E. Fahrbach, V. V. Ivanov, S. Østerhus, D. Quadfasel, U. Schauer, V. Tverberg, and R. A. Woodgate (2000), Water mass distribution in Fram Strait and over the Yermak Plateau in summer 1997, *Ann. Geophys.*, *18*, 687–705, doi:10.1007/s00585-000-0687-5.

Sallarès, V., B. Biescas, G. Buffett, R. Carbonell, J. J. Dañobeitia, and J. L. Pelegrí (2009), Relative contribution of temperature and salinity to ocean acoustic reflectivity, *Geophys. Res. Lett.*, *36*, L00D06, doi:10.1029/2009GL040187.

Saloranta, T. M., and P. M. Haugan (2004), Northward cooling and freshening of the warm core of the West Spitsbergen Current, *Polar Res.*, *23*, 79–88, doi:10.1111/j.1751-8369.2004.tb00131.x.

Saloranta, T. M., and H. Svendsen (2001), Across the Arctic front west of Spitsbergen: High-resolution CTD sections from 1998-2000, *Polar Res.*, *20*(2), 177–184, doi:10.1111/j.1751-8369.2001.tb00054.x.

Sarkar, S., C. Berndt, A. Chabert, D. G. Masson, T. A. Minshull, and G. K. Westbrook (2011), Switching of a paleo-ice stream in northwest Svalbard, *Quat. Sci. Rev.*, *30*(13–14), 1710–1725, doi:10.1016/j.quascirev.2011.03.013.

Schauer, U., E. Fahrbach, S. Osterhus, and G. Rohardt (2004), Arctic warming through the Fram Strait: Oceanic heat transport from 3 years of measurements, *J. Geophys. Res.*, *109*, C06026, doi:10.1029/2003JC001823.

Schlichtholz, P., and M. N. Houssais (2002), An overview of the theta-S correlations in Fram Strait based on the MIZEX 84 data, *Oceanologia*, *44*(2), 243–272.

Sheen, K. L., N. J. White, and R. W. Hobbs (2009), Estimating mixing rates from seismic images of oceanic structure, *Geophys. Res. Lett.*, *36*, L00D04, doi:10.1029/2009GL040106.

Sheen, K. L., N. J. White, C. P. Caulfield, and R. W. Hobbs (2012), Seismic imaging of a large horizontal vortex at abyssal depths beneath the Sub-Antarctic Front, *Nat. Geosci.*, *5*(8), 542–546, doi:10.1038/ngeo1502.

Sheriff, R. E., and L. P. Geldart (1995), *Exploration Seismology*, 2nd ed., 592 pp., Cambridge Univ. Press, Cambridge, U. K.

Sirevaag, A., and I. Fer (2009), Early spring oceanic heat fluxes and mixing observed from drift stations north of Svalbard, *J. Phys. Oceanogr.*, *39*, 3049–3069, doi:10.1175/2009JPO4172.1.

Smith, K. S., and R. Ferrari (2009), The production and dissipation of compensated thermohaline variance by mesoscale stirring, *J. Phys. Oceanogr.*, *39*, 2477–2501, doi:10.1175/2009JPO4103.1.

Steele, E., T. Boyd, M. Inall, E. Dumont, and C. Griffiths (2012), Cooling of the West Spitsbergen Current: AUV-based turbulence measurements west of Svalbard, in *2012 IEEE/OES Autonomous Underwater Vehicles (AUV)*, vol. 1, pp. 1–7, IEEE, Southampton, U. K., doi:10.1109/AUV.2012.6380741.

Teigen, S. H., F. Nilsen, and B. Gjevik (2010), Barotropic instability in the West Spitsbergen Current, *J. Geophys. Res.*, *115*, C07016, doi:10.1029/2009JC005996.

Thorpe, S. (2005), *The Turbulent Ocean*, 437 pp., Cambridge Univ. Press, Cambridge, U. K.

Torres-Valdés, S., T. Tsubouchi, S. Bacon, A. C. Naveira-Garabato, R. Sanders, F. A. McLaughlin, B. Petrie, G. Kattner, K. Azetsu-Scott, and T. E. Whitledge (2013), Export of nutrients from the Arctic Ocean, *J. Geophys. Res. Oceans*, *118*, 1625–1644, doi:10.1002/jgrc.20063.

Untersteiner, N. (1988), On the ice and heat balance in Fram Strait, *J. Geophys. Res.*, *93*(C1), 527–531, doi:10.1029/JC093iC01p00527.

Vlasenko, V., N. Stashchuk, K. Hutter, and K. Sabinin (2003), Nonlinear internal waves forced by tides near the critical latitude, *Deep Sea Res., Part I*, *50*(3), 317–338, doi:10.1016/S0967-0637(03)00018-9.

Westbrook, G. K., et al. (2009), Escape of methane gas from the seabed along the West Spitsbergen continental margin, *Geophys. Res. Lett.*, *36*, L15608, doi:10.1029/2009GL039191.